

Patterns of deformation in the deepest mantle linked to ancient subduction

Jonathan Wolf^{1,2,*}, Barbara A. Romanowicz¹, Edward Garnero³, Weiqiang Zhu¹, and John D. West³

¹Department of Earth and Planetary Science, University of California, Berkeley, CA, USA

²Miller Institute for Basic Research in Science, Berkeley, CA, USA

³School of Earth and Space Exploration, Arizona State University, Tempe, AZ, USA

*jonathan.wolf@berkeley.edu

ABSTRACT

Shear wave speeds in Earth's deepest mantle (D'') that vary with wave propagation and polarization direction – a property called seismic anisotropy – offer insights into mantle convection. To date, global patterns of D'' anisotropy have been mostly derived from long wavelength radially anisotropic tomography models, which often disagree except for the large-scale degree-2 pattern. Here, we present 70,000 differential splitting measurements from seismic waves that traverse Earth's mantle and core, sampling nearly 75% of D'' , including most seismically faster regions. We conduct detailed synthetic tests to demonstrate which splitting measurements indicate the presence of lowermost mantle anisotropy. Evidence for D'' anisotropy is found in about two thirds of our sampled area, more than doubling the area in which seismic anisotropy has been detected using shear-wave splitting measurements. Inferred deformation is strong within and around ancient slab remnants, which likely have lower temperatures than the ambient mantle. This is consistent with the crystallographic orientation of postperovskite (pPv) being an important contributor to the new maps of lowermost mantle anisotropy. Our observations suggest a close link between the subduction of tectonic plates and convective flow in the deepest mantle.

Main

Convective flow within Earth's mantle leads to deformation of mantle materials¹⁻³. The deformed materials often develop a property called seismic anisotropy, for which shear wave velocities depend on

the polarization and/or propagation direction of the wave. Therefore, seismic anisotropy is perhaps the most direct indicator of deep mantle flow that can be exploited in the Earth Sciences²⁻⁴.

Strong seismic anisotropy has been observed in the transition zone and at shallower depths^{5,6}, the uppermost lower mantle in subduction zones⁷, and the lowermost 100s of km of the mantle^{2,3} (the latter also referred to as D''), whereas the majority of the lower mantle is almost isotropic^{8,9}. Seismic anisotropy in the lowermost mantle is commonly investigated through regional shear-wave splitting studies¹⁰⁻¹² or through global inversions for radially anisotropic structure¹³⁻¹⁵. The global models generally agree that vertically polarized shear waves travel faster than horizontally polarized ones within the two antipodal large low-velocity provinces (LLVPs) in Earth's mantle, while the opposite occurs in surrounding areas²; however, there are considerable regional discrepancies among the global models². Shear-wave splitting studies can reveal changes in seismic anisotropy on shorter lateral scales (100s of km) than global inversions for radial anisotropy, but have yet to be applied to most lowermost mantle regions¹⁶.

It is not yet established if the strength of lowermost mantle anisotropy is associated in a systematic fashion with specific deep mantle structures. For example, while regional studies frequently find strong anisotropy at LLVP edges^{10,17}, D'' anisotropy appears as likely to be found near them as elsewhere¹⁶. Second, seismic anisotropy patterns within LLVPs, which constitute roughly 30% of the area of the core mantle boundary¹⁸, have not been well-studied^{2,3}, primarily because of limitations in global ray coverage¹⁶. Finally, the degree to which seismic anisotropy is caused by different flow phenomena is not resolved, e.g., roots of plume-like upwellings^{19,20}, flow associated with margins of LLVPs^{10,17}, or areas where slabs impact the core-mantle boundary (CMB)^{11,21}, all of which have previously been suggested. In this study, we demonstrate that deformation outside the LLVPs is primarily linked to subduction processes and subducted slab remnants, which may also partially account for the seismic anisotropy observed at LLVP edges. This observed seismic anisotropy can be plausibly explained by crystallographic orientation of pPv. We also present measurements of seismic anisotropy within a portion of the African LLVP, although LLVP regions remain dominantly unsampled.

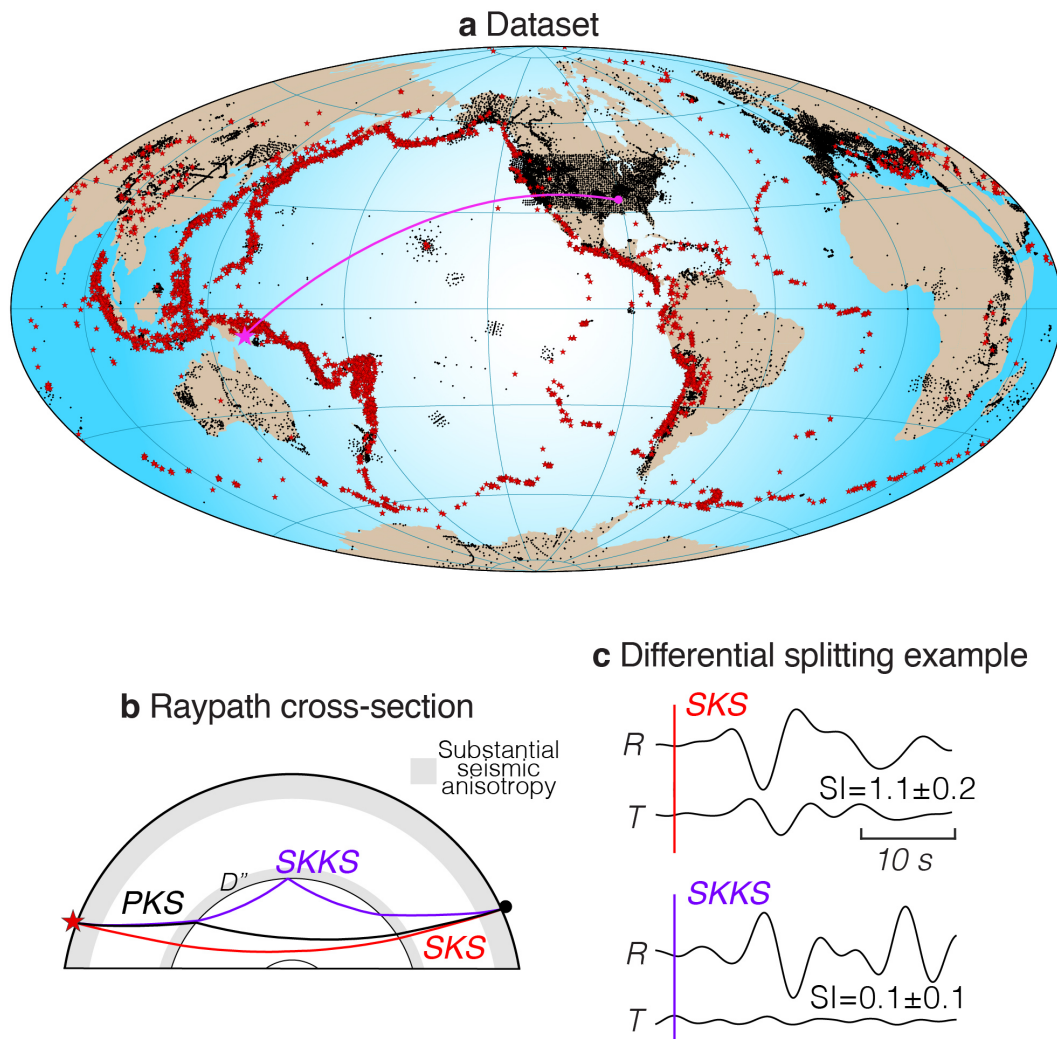


Figure 1. Source-receiver configuration, Earth cross-section, and example differential splitting measurement. **a** Stations (black circles) and events (red stars) used in the study. Data are from over 4,700 events and 25,000 stations. The magenta star, circle, and line denote the event, station, and great-circle path for the measurement shown in **c**. **b** Cross-section showing SKS, PKS, and SKKS (*KS) raypaths from the source (red star) to the station (black circle), sampling seismic anisotropy in the upper and lowermost mantle (gray). **c** SKS and SKKS radial (R) and transverse (T) seismograms at station Y43A. Predicted arrival times from PREM²² are marked by vertical red (SKS) and violet (SKKS) lines. *KS shows strong splitting ($SI = 1.1$), while SKKS splitting is null ($SI = 0.1$), demonstrating strong differential splitting between the two phases.

Shear-wave splitting approach

A common approach to detecting lowermost mantle anisotropy is to compare the splitting intensities (SI , see Online Methods) of SKS and SKKS, or PKS and SKKS phases (Figure 1b)^{8,23}, hereafter referred to as *KS differential splitting. This method is effective because the lateral raypath separation distance between SKS and SKKS (or PKS and SKKS) is more substantial in the lowermost mantle (Supplementary

Figure S1) compared to being nearly identical in the upper mantle (and most of the lower mantle is nearly isotropic; Figure 1b). A complication arises as the slight differences in upper mantle sensitivity between *KS pairs can sometimes still contribute to differential splitting²⁴. To mitigate this, measurements with only small differences in a quantity called the splitting intensity (see Online Methods) are not utilized in this paper as evidence for seismic anisotropy in D''.

Tests of the *KS differential splitting technique have been previously conducted only for individual source-receiver pairs and a single layer of seismic anisotropy of global lateral extent in the upper mantle^{24,25}. Such a simplified scenario does not consider seismic anisotropy changes as a function of depth and lateral position. Therefore, in this work, we implement a test for depth and laterally dependent upper mantle and transition zone anisotropy²⁶, and show that for our approach $|\delta SI|$ -values above 0.4 can be safely regarded as evidence for anisotropy deeper than the transition zone (Online methods; Figure M1).

We analyze *KS differential splitting (see Online Methods) using a global dataset of 16 million three-component seismograms, which sample approximately 75% of the D'' region (Figure 1). An example SKS-SKKS differential splitting measurement is shown in Figure 1c, taken from an event that occurred on September 5, 2011, and was recorded at station Y43A (Figure 1a). In this case, the SKKS phase is almost unsplit ($SI = 0.1$), whereas SKS is clearly split ($SI = 1.2$), indicating that at least one of the phases is influenced by D'' anisotropy (see Supplementary Figure S2 for an example of a PKS-SKKS differential measurement).

Global ray sampling

The D'' coverage of *KS pairs for which well-constrained (see Online methods) $|\delta SI|$ measurements are obtained is shown in Figure 2a. The plotting convention (see Figure 2, inset) is such that lines connect the horizontal distance (viewed from above) between *KS pierce points at the CMB and the top of the layer (assuming a D'' thickness of 250 km). For SKS-SKKS pairs, for example, these lines connect the pierce point of SKKS through the CMB, and the SKS pierce point through the upper boundary of D'', approximating the distance along the great-circle path that differential splitting measurements are sensitive to (neglecting finite frequency effects). In the following, we will refer to these lines as the pierce point connecting segments.

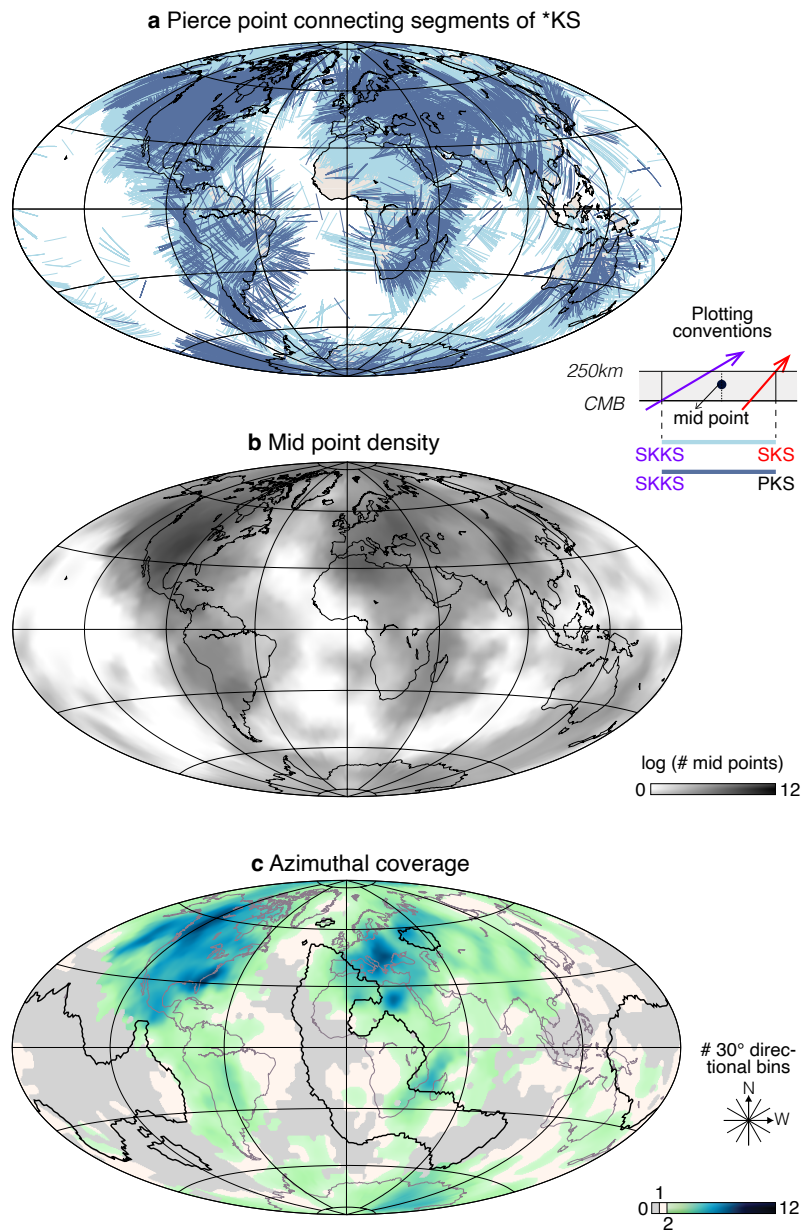


Figure 2. Ray coverage in this study. **a** Pierce point connecting segments for SKKS-SKKS (light blue) and PKS-SKKS pairs (dark blue). The inset explains the plotting convention: Pierce point connecting segments link the SKKS pierce point through the CMB with the SKS (or PKS) pierce point through the upper D'' boundary, assumed here to be 250 km above the core-mantle boundary. Arrows through D'' indicate SKKS (violet) and SKS (red) raypaths. The midpoint of the pierce point connecting segment is shown as a black circle. **b** Density of pierce point connecting segment midpoints (legend) binned on a $4^\circ \times 4^\circ$ D'' grid, shown on a log scale due to high station density across North America. **c** Azimuthal coverage, shown as the number of 30° directional intervals with more than seven measurements sampled per $4^\circ \times 4^\circ$ D'' bin (legend). Gray indicates no ray coverage. Thick black outlines denote regions where three of five models from a cluster analysis¹⁸ suggest low seismic velocities (i.e., LLVPs).

The midpoint sampling density of these pierce point connecting segments in D'' is shown in Figure 2b. A logarithmic scale is used due to the highly variable global ray coverage, and we use a D'' bin size of $4^\circ \times 4^\circ$. Overall, our data sample nearly 75% of D'' globally. We also show azimuthal sampling in Figure 2c, represented by the number of 30° directional intervals relative to geographic north (Figure 2c, inset) that are sampled by at least seven δSI measurements. We note that there is a different angle relative to the anisotropy whether *KS pairs sample D'' from an azimuth of, for example, 0° or 180° , which is why the maximum number of 30° intervals that a D'' location can be sampled from is 12. We consistently use this binning approach in the following.

Globally widespread seismic anisotropy of the deepest mantle

Some previous studies have interpreted differential splitting as evidence for a gradient in D'' anisotropy¹⁹ because *KS pairs sample different portions of D'' (Figure 1b). However, this does not account for the different angles at which *KS pairs travel through the lowermost mantle (Figure 1b)³. The magnitude of $|\delta SI|$ is thus influenced by both the overall strength of D'' anisotropy and its lateral gradient, but differential measurements do not provide enough information to distinguish these factors. Therefore, in this study, our general interpretation is that $|\delta SI| > 0.4$ indicates the presence of D'' anisotropy (and not necessarily a gradient).

Figure 3a shows $|\delta SI|$ values using the midpoint of the pierce point connecting segment (Figure 2) to project them to the lowermost mantle. The binning approach described above is used and we show $|\delta SI|$ values from the 30° directional interval with the largest $|\delta SI|$ average. The color scale is such that regions where these $Max(|\delta SI|)$ -values are lower than or equal to 0.4 are colored white, where D'' anisotropy is not clearly constrained. For larger maximum $|\delta SI|$ -values, which indicate the presence of lowermost mantle anisotropy (Online Methods), red colors are used; $Max(|\delta SI|)$ up to 1.6 are detected. Overall, two-thirds the covered bins show $Max(|\delta SI|) > 0.4$, while approximately a quarter of D'' , mostly within the LLVPs, is not covered. Compared to where the presence of D'' anisotropy has been suggested in previous regional studies, our results more than double the total D'' area in which the presence of lowermost mantle anisotropy is detected (Figure 3b).

Using *KS splitting analyses, we find seismic anisotropy in almost all areas in which seismic anisotropy

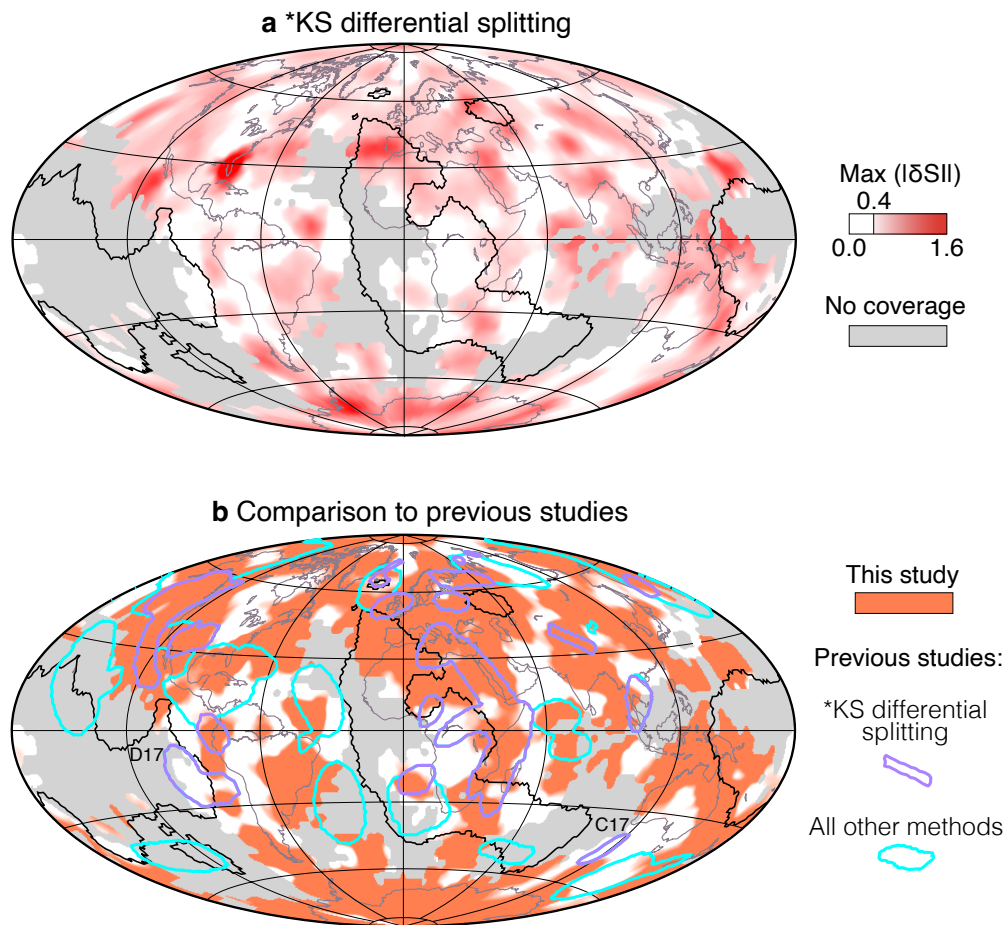


Figure 3. D'' anisotropy results. **a** The color scale (legend) shows maximum δSI values (across all directional swaths) for each D'' bin ($4^\circ \times 4^\circ$). White colors represent D'' regions with $|\delta SI| < 0.4$. Unsamplered regions are shown by gray shading. Thick black lines indicate where three out of five models suggest low seismic velocities in a cluster analysis¹⁸ (i.e., LLVPs). **b** Plotting conventions are similar to panel **a**, except that regions with maximum δSI values are colored orange, and outlines of anisotropy locations determined in previous shear-wave splitting studies are shown. Anisotropic regions suggested in all previous studies are shown as cyan outlines. Violet outlines (plotted on top of the cyan outlines) indicate regions where the presence of lowermost mantle anisotropy has been inferred using *KS differential splitting. The regions in which seismic anisotropy was detected by Creasy et al. (2017)²⁷ (C17) and Deng et al. (2017)²⁸ (D17) are labeled (and further discussed in the text).

has previously been suggested¹⁶. The only two differential splitting studies with which our results appear to disagree are from Deng et al. (2017)²⁸ and Creasy et al. (2017)²⁷ (Figure 3), which both interpreted the relatively low δSI (< 0.4) values and the small-scale variations of them as evidence for the lowermost mantle anisotropy, whereas in this study we choose a threshold of 0.4. Our measurements also show evidence for seismic anisotropy in many regions that have been suggested using techniques other than *KS differential splitting. Perfect agreement with these studies is not necessarily expected because phase

other than *KS are sensitive to the anisotropy in a different way. Additionally, several potential concerns have been noted with some of the techniques used in these studies^{29–31}. However, it worth pointing out that there is a good agreement of our results with previous S_{diff} splitting results, especially those that avoid ambiguities due to the source polarization^{10,12,32}, which have been suggested to be a potential contaminating factor^{30,33}. S_{diff} splitting measurements generally indicate $V_{SH} > V_{SV}$ in the fast regions of the lowermost mantle, consistent with global inversions for seismic anisotropy with radial symmetry^{13–15}.

Deformation in slab-dominated regions

Candidate regions that host ancient slab remnants are usually colder than the surrounding mantle, leading to enhanced seismic wave speeds^{36–38}. The combination of constraints from paleographic plate reconstructions and seismic tomography has helped to identify several slab remnants in the deepest mantle (Figure 4b)^{36,37}. We sample from multiple directions the locations of 13 of these slabs that reach below a depth of 2500 km (Figure 4a). These locations coincide with regions of strong seismic anisotropy and therefore strong deformation. The only slab base for which we do not find strong evidence for seismic anisotropy is the Trans Americas Anomaly (Figure 4b). This location is where previous work²⁸ found evidence for seismic anisotropy using SKS-SKKS differential splitting with a lower differential threshold than this work to identify seismic anisotropy. D'' anisotropy may therefore be present but below the confidence level we have set in our global scale analysis.

We find distinct patches of seismic anisotropy that coincide with previously suggested locations of ancient slab remnants, for example at the base of the Al Jawf, Beaufort, Central China, Cocos, Georgia Islands, and Sao Francisco anomalies³⁶ (Figure 4b). Of these five, only the base of the Central China Slab³² and, partially, the Al Jawf Anomaly¹⁷ have been previously associated with D'' anisotropy. In other cases, lowermost mantle areas that mark remnant slab locations are merged with anisotropic regions larger than a single slab's extent, for example in case of the Balkan, Mongol-Okhotsk and Wichita anomalies. The latter region may be part of a patch of seismic anisotropy that has been previously suggested to include material from the Farallon Slab^{11,21,37} (Figure 4b, dashed outline).

Comparisons of seismic anisotropy locations to wavespeed anomalies from tomography models are often conducted. Figure 4b shows a comparison between our anisotropy results and a vote map of higher

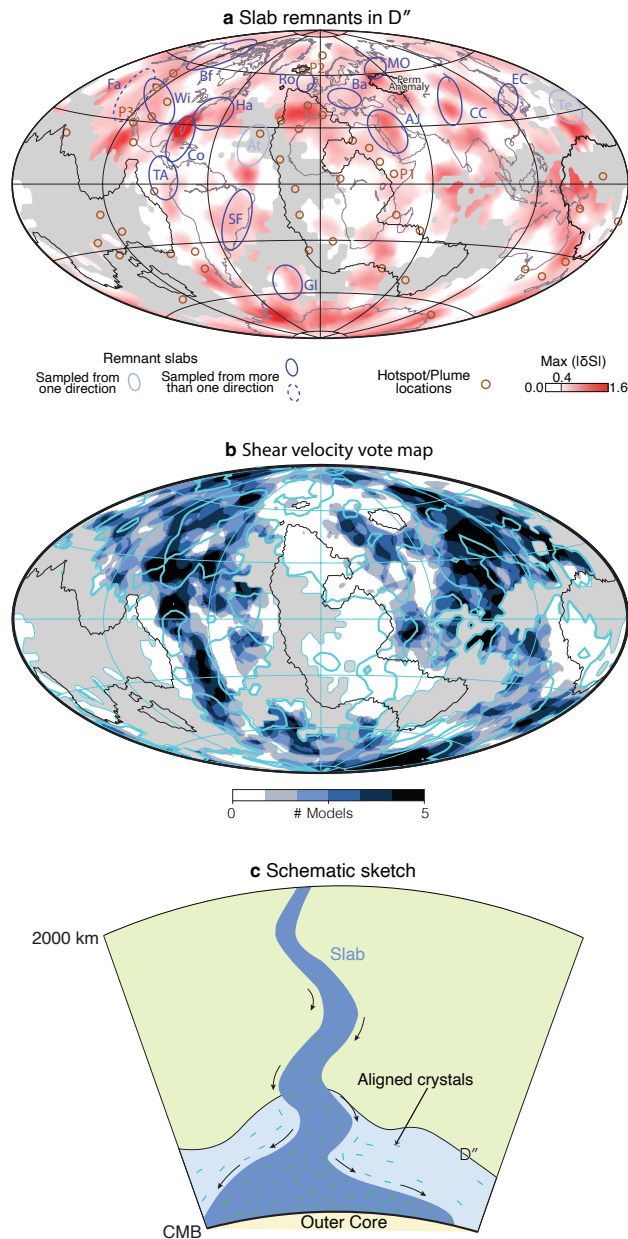


Figure 4. Comparisons to ancient slab locations and seismic tomography. **a** Seismic anisotropy results using the plotting conventions in Figure 3a. Hotspot/plume locations from Steinberger (2000)³⁴ and French and Romanowicz (2015)³⁵, and slab remnant regions from van der Meer et al. (2018)³⁶ (solid outlines) and Asplet et al. (2020)¹¹ (dashed outline) are shown (see legend). The Afar (P1), Iceland (P2) and Yellowstone (P3) plumes are labeled. Slab abbreviations³⁶: AJ: Al Jawf; Atlantis: At; Balkan: Ba; Beaufort: Bf; Central China: CC; Cocos: Co; East China: EC; Farallon: Fa; Georgia Islands: GI; Hatteras: Ha; Mongol-Okhotsk: MO; Rockall: Ro; Sao Francisco: SF; Telkhinia: Te; Trans Americas: TA; Wichita: Wi. **b** Top: Comparison of $\delta|S| > 0.4$ outlines (cyan) to a vote map of above-average shear velocity at 2800 km depth (see legend, for additional details see Supplementary Information). **c** Schematic of deep mantle deformation induced by a sinking slab (dark blue), leading to crystal alignment (black sticks) and strong seismic anisotropy. A post-perovskite layer is expected to be thicker in cooler mantle regions.

than average velocities from five tomography models (Supplementary Information). It is apparent that we sample the lowermost mantle in most of the high-velocity regions, and that seismic anisotropy is widespread within them. Many of these regions have been associated with specific ancient slab remnants (Figure 4a), although not all of them. We also find previously not detected (Figure 3a,b) seismic anisotropy in parts of the African LLVP, although we cannot draw conclusions about the nature and cause of seismic anisotropy within the LLVPs which are largely unsampled.

Findings from previous regional studies have often been associated with a change of flow regime at the edge of LLVPs^{10,17,19,23}. In many of these regions, such as the eastern edge of the African LLVP, we also find evidence for strong seismic anisotropy (Figure 3a), though the magnitude of the $|\delta SI|$ -values varies. On a global scale, however, no strong trends exist between the magnitude of $|\delta SI|$ and lateral velocity gradients in seismic tomography models (Supplementary Figure S3). In multiple regions in which seismic anisotropy has been found near LLVP edges, it may be explained by deformation caused by ancient slab remnants (Figure 4a). The same is true for seismic anisotropy near the Perm anomaly^{39,40} (Figure 4a).

Additionally, to varying degrees, we detect seismic anisotropy near deep mantle plume roots that have been associated with strong deformation, for example, Afar¹⁹, Iceland⁴¹ and Yellowstone²⁰ (Figure 4a). However, the lateral extent of basal upwellings may be local and limited, and improved anisotropy constraints from multiple seismic phases may be necessary to conclusively attribute seismic anisotropy patterns to them.

Our differential *KS splitting measurements are not suitable to infer the precise orientation of the detected seismic anisotropy. However, in slab-dominated regions, a combination of two mechanisms appears likely. First, fossil anisotropy may be present within the slab inherited from previous episodes of deformation (Figure 4c). Given that the presence of seismic anisotropy has now been substantiated in the uppermost lower mantle⁷ and the lowermost mantle in slab-dominated regions, some of the anisotropic signature may be preserved as slabs sink through the lower mantle. However, substantial uncertainties remain regarding how anisotropic fabric is inherited across phase transitions^{2,42}. Second, as slabs enter the lowermost mantle, they deform the surrounding material and undergo substantial deformation themselves as they reach the CMB and broaden⁴²⁻⁴⁴ (Figure 4c). This, in turn, may lead to substantial seismic anisotropy within and around the slab-dominated regions.

The composition and elastic properties of the lowermost mantle remain subjects of debate. For example, it is unclear whether bridgmanite's high-pressure polymorph pPv is present everywhere above the CMB^{2,45}. The lowermost mantle regions dominated by ancient slab remnants, however, likely have lower temperatures than the ambient mantle, implying a relatively shallow bridgmanite-pPv transition⁴⁶. Indeed, multiple previous studies have suggested that their anisotropy results in the seismically faster regions are consistent with crystallographic preferred orientation of pPv^{11, 12, 42–44}. Additionally, recent work⁴⁷ has demonstrated that pPv anisotropy at the base of slabs can explain both discrepant *KS splitting and a dominant $V_{SH} > V_{SV}$ pattern (as suggested by radial anisotropy and S_{diff} measurements) inferred from geodynamic flow models. Moreover, mineral physics results suggest that strain values above 0.5 can cause detectable D'' anisotropy in pPv⁴⁸, and recent geodynamic flow modeling results^{49,50} predict depth-averaged strain values above that threshold in almost all regions globally. Taken together, this makes the crystallographic orientation of pPv the likely dominant contributor to the measured seismic anisotropy.

By more than doubling the area in which seismic anisotropy has been detected using shear-wave splitting, we show that deformation in the lowermost mantle is widespread, with a dominant pattern of seismic anisotropy coinciding with locations of ancient slab remnants. In these relatively cold mantle domains, the strong seismic anisotropy is likely caused by crystallographic orientation of postperovskite. This confirms an intimate link between surface subduction processes and deformation in the lowermost mantle via whole mantle convection.

Online Methods

Shear-wave splitting measurements

Upon their conversion from P-to-S as they reenter the mantle from the core (Figure 1b), *KS waves become fully SV-polarized. If seismic anisotropy is present along the mantle raypath on the receiver side, energy is split to the transverse component $T(t)$, and the $T(t)$ pulse shape will resemble the radial component time derivative $R'(t)$ ^{51,52}. The splitting intensity (SI)⁵³ takes advantage of this and, for *KS waves, can be expressed as:

$$SI = -2 \frac{T(t)R'(t)}{|R'(t)|^2}. \quad (1)$$

We use global seismic data for events with moment magnitudes 5.9 or higher that occurred after January 1, 2000, from 24 different datacenters (networks and their citations are provided in the Supplementary Information) as shown in Figure 1a. This dataset contains 16 million three-component seismograms. The data are instrument-deconvolved, rotated to radial and transverse components (based on station metadata), and then bandpass-filtered to retain periods between 6 and 25 s.

We measure the *KS splitting intensities from our dataset using a modified version of SplitRacer_auto⁵⁴. The modifications do not affect the core functionality of SplitRacer_auto but make it substantially faster, which is helpful given the large data volume used in this study. For more details on our measurement approach, we refer the reader to Wolf et al. (2024)⁵⁵. We only retain *SI* measurements with 95% confidence intervals⁵³ smaller than ± 0.4 . In cases of strong splitting, *SI* may not be additive, implying that stronger anisotropy does not necessarily lead to larger *SI* values at the periods used²⁵. To avoid such effects, we only use *KS with absolute splitting intensities below 1.5.

Synthetic tests for method verification

We conduct a synthetic test, with the aim of determining from what threshold δSI between *KS phase pairs measurements are indicative of lowermost mantle anisotropy. Such tests have been conducted before for individual source-receiver pairs and a single layer of seismic anisotropy in the upper mantle of global lateral extent²⁴. Such a simplified scenario is not realistic for Earth because seismic anisotropy changes both as a function of depth and lateral position. Additionally, in this study we do not focus on every single event-station pair individually but bin our measurements.

We conduct synthetic simulations using AxiSEM3D⁵⁶ down to a minimum period of 5 s, incorporating both ellipticity and attenuation. We use Fourier coefficients of the 3-D wavefield within 2-D meridian domain of up to 200, and verify this choice using wavefield scanning⁵⁶. The station locations correspond to those of the Transportable Array⁵⁷, with six events simulated at equal azimuthal intervals around the continental United States (Figure M1, inset). For each event, we select the CMTSOLUTION⁵⁸ for an earthquake that occurred on July 3, 2012 (Cook Strait, New Zealand), assuming a depth of 500 km. For *KS splitting measurements, these specific source details are generally not important, as the radial polarization of *KS results from the P-to-SV conversion at the CMB.

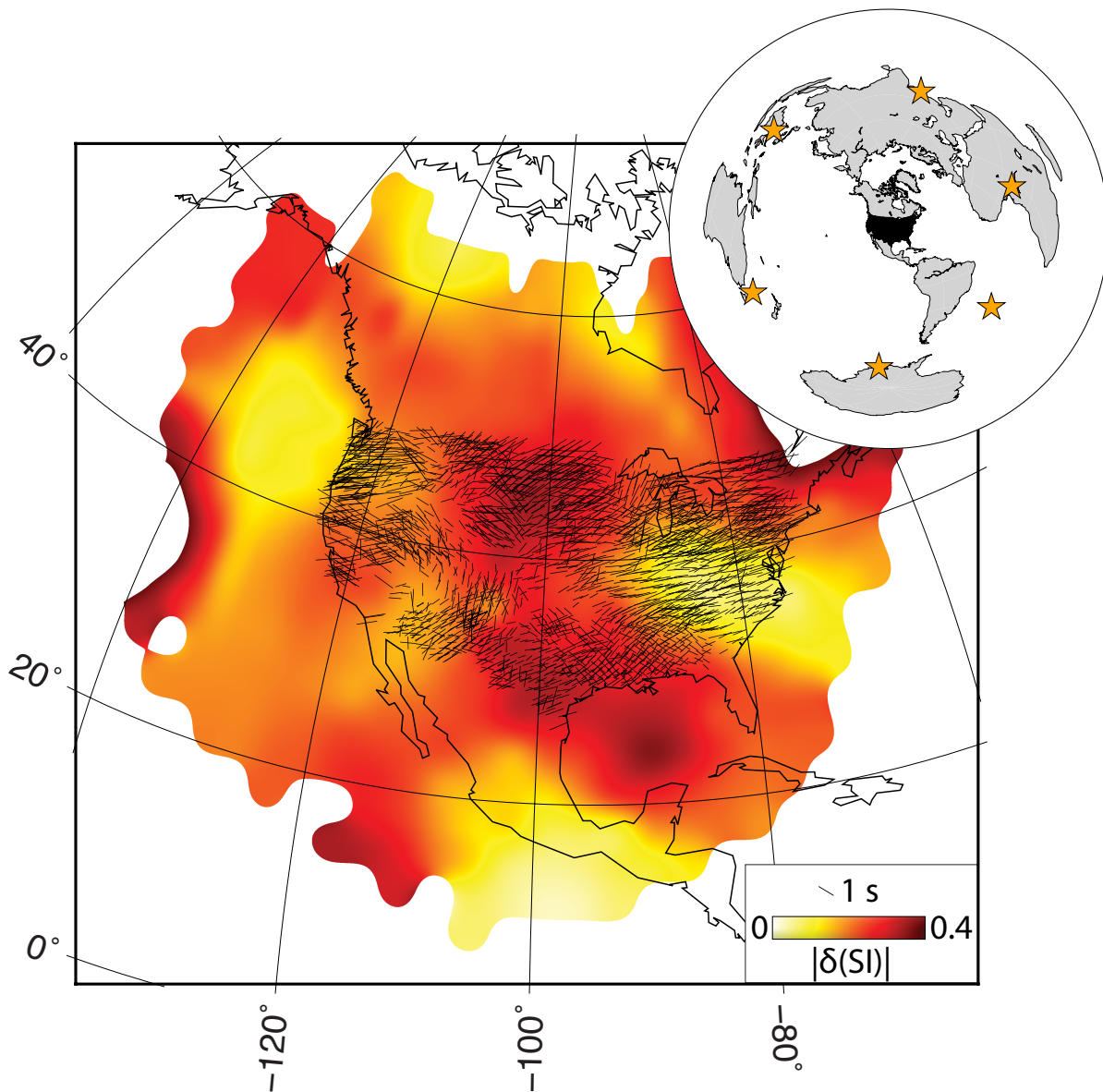


Figure M1. Synthetic test to determine what differential splitting values can be explained by effects of seismic anisotropy in the upper mantle and transition zone. We incorporate the model of Yuan and Romanowicz (2010)²⁶ across North America (see Online Methods). Inset: Source-receiver configuration. Events are represented as yellow stars and stations (across the United States) as black circles. Main panel: Background colors represent differential SKS-SKKS splitting intensities (legend), projected to the mid point of the pierce point connecting segment (Figure 2a, inset) in the lowermost mantle. Results are binned in $4^\circ \times 4^\circ$ bins, and we show the largest average δSI value across all 30° directional swaths for every D'' bin (see text). Individual fast direction and delay time measurements from SKS are shown as black sticks (legend).

Our background model is isotropic PREM²², with seismic anisotropy added to the upper 650 km of the mantle beneath the contiguous United States. Specifically, we implement the azimuthal anisotropy model from Yuan and Romanowicz (2010)²⁶, which is based on surface wave dispersion and shear-wave

splitting data. The model includes both radial and azimuthal anisotropy, with two to three layers of the latter, each with a different fast axis direction, mapped beneath the North American continent. At each depth-latitude-longitude point, we utilize the olivine A-type elastic tensor from Karato (2008)⁵⁹, and use MSAT⁶⁰ to mix it with its isotropic projection⁶¹, achieving the anisotropy strength as reported by Yuan and Romanowicz (2010). We then rotate the olivine elastic tensor around the vertical axis (assuming horizontal simple shear) to align with the fast polarization direction indicated by Yuan and Romanowicz (2010), under the assumption of vertically propagating *KS waves. This results in an anisotropic upper mantle with realistic elastic tensor values that vary both laterally and with depth. Since the model by Yuan and Romanowicz (2010) underestimates *KS splitting strengths, we double the anisotropy strength everywhere.

We process the synthetic seismograms in the same way as the real data, following the setup described in the Online Methods section. The resulting average splitting intensities across the United States from the synthetic simulation (with doubled anisotropy strength) are comparable to those of the real data. We compute differential SKS-SKKS splitting intensities and project them to the lowermost mantle, as done for the real data (Figure M1). This approach allows us to assess which $|\delta SI|$ values may arise solely from upper mantle anisotropy. We bin $|\delta SI|$ values projected to the midpoint of the pierce point connecting segment (Figure 2, inset) in 30° directional intervals with respect to geographic north. Given the directional dependency of seismic anisotropy, if interpreting δSI values in terms of lowermost mantle anisotropy, one should consider the directional interval with the highest average $|\delta SI|$ (projected onto D'') to determine anisotropy presence. We take the maximum across all directional intervals with more than seven measurements per D'' bin. While precise $Max(|\delta SI|)$ values vary by bin, values are consistently < 0.4 , suggesting that $Max(|\delta SI|) > 0.4$ reliably indicates the presence of D'' anisotropy for our processing scheme.

References

1. Long, M. D. & Becker, T. Mantle dynamics and seismic anisotropy. *Earth Planet. Sci. Lett.* **297**, 341–354, DOI: [10.1016/j.epsl.2010.06.036](https://doi.org/10.1016/j.epsl.2010.06.036) (2010).

2. Romanowicz, B. & Wenk, H.-R. Anisotropy in the deep Earth. *Phys. Earth Planet. Interiors* **269**, 58–90, DOI: [10.1016/j.pepi.2017.05.005](https://doi.org/10.1016/j.pepi.2017.05.005) (2017).
3. Wolf, J., Li, M., Long, M. D. & Garnero, E. Advances in mapping lowermost mantle convective flow with seismic anisotropy observations. *Rev. Geophys.* **62**, e2023RG000833, DOI: [10.1029/2023RG000833](https://doi.org/10.1029/2023RG000833) (2024).
4. Nowacki, A., Wookey, J. & Kendall, J.-M. New advances in using seismic anisotropy, mineral physics and geodynamics to understand deformation in the lowermost mantle. *J. Geodyn.* **52**, 205–228, DOI: [10.1016/j.jog.2011.04.003](https://doi.org/10.1016/j.jog.2011.04.003) (2011).
5. Savage, M. K. Seismic anisotropy and mantle deformation: What have we learned from shear wave splitting? *Rev. Geophys.* **37**, 65 – 106, DOI: [10.1016/10.1029/98RG02075](https://doi.org/10.1016/10.1029/98RG02075) (1999).
6. Beghein, C., Resovsky, J. & van der Hilst, R. D. The signal of mantle anisotropy in the coupling of normal modes. *Geophys. J. Int.* **175**, 1209–1234, DOI: [10.1111/j.1365-246X.2008.03970.x](https://doi.org/10.1111/j.1365-246X.2008.03970.x) (2008).
7. Ferreira, A., Faccenda, M., Sturgeon, W., Chang, S.-J. & Schardong, L. Ubiquitous lower-mantle anisotropy beneath subduction zones. *Nat. Geosci.* **12**, 301—306, DOI: [10.1038/s41561-019-0325-7](https://doi.org/10.1038/s41561-019-0325-7) (2019).
8. Niu, F. & Perez, A. M. Seismic anisotropy in the lower mantle: A comparison of waveform splitting of SKS and SKKS. *Geophys. Res. Lett.* **31**, DOI: [10.1029/2004GL021196](https://doi.org/10.1029/2004GL021196) (2004).
9. Meade, C., Silver, P. G. & Kaneshima, S. Laboratory and seismological observations of lower mantle isotropy. *Geophys. Res. Lett.* **22**, 1293–1296, DOI: [10.1029/95GL01091](https://doi.org/10.1029/95GL01091) (2005).
10. Cottaar, S. & Romanowicz, B. Observations of changing anisotropy across the southern margin of the African LLSVP. *Geophys. J. Int.* **195**, 1184–1195, DOI: [10.1093/gji/ggt285](https://doi.org/10.1093/gji/ggt285) (2013).
11. Asplet, J., Wookey, J. & Kendall, M. A potential post-perovskite province in D'' beneath the Eastern Pacific: evidence from new analysis of discrepant SKS–SKKS shear-wave splitting. *Geophys. J. Int.* **221**, 2075–2090, DOI: [10.1093/gji/ggaa114](https://doi.org/10.1093/gji/ggaa114) (2020).
12. Wolf, J. & Long, M. D. Slab-driven flow at the base of the mantle beneath the northeastern Pacific Ocean. *Earth Planet. Sci. Lett.* **594**, 117758, DOI: [10.1016/j.epsl.2022.117758](https://doi.org/10.1016/j.epsl.2022.117758) (2022).

13. Panning, M. & Romanowicz, B. Inferences on flow at the base of earth's mantle based on seismic anisotropy. *Science* **303**, 351–353, DOI: [10.1126/science.1091524](https://doi.org/10.1126/science.1091524) (2004).
14. Auer, L., Boschi, L., Becker, T. W., Nissen-Meyer, T. & Giardini, D. Savani: A variable resolution whole-mantle model of anisotropic shear velocity variations based on multiple data sets. *J. Geophys. Res. Solid Earth* **119**, 3006–3034 (2014).
15. Chang, S.-J., Ferreira, A. M. G., Ritsema, J., van Heijst, H. J. & Woodhouse, J. H. Joint inversion for global isotropic and radially anisotropic mantle structure including crustal thickness perturbations. *J. Geophys. Res. Solid Earth* **120**, 4278–4300, DOI: [10.1002/2014JB011824](https://doi.org/10.1002/2014JB011824) (2015).
16. Wolf, J., Long, M. D., Li, M. & Garnero, E. Global compilation of deep mantle anisotropy observations and possible correlation with low velocity provinces. *Geochem. Geophys. Geosystems* **24**, e2023GC011070, DOI: [10.1029/2023GC011070](https://doi.org/10.1029/2023GC011070) (2023).
17. Reiss, M. C., Long, M. D. & Creasy, N. Lowermost Mantle Anisotropy Beneath Africa From Differential SKS-SKKS Shear-Wave Splitting. *J. Geophys. Res. Solid Earth* **124**, 8540–8564, DOI: [10.1029/2018JB017160](https://doi.org/10.1029/2018JB017160) (2019).
18. Lekic, V., Cottaar, S., Dziewonski, A. & Romanowicz, B. Cluster analysis of global lower mantle tomography: A new class of structure and implications for chemical heterogeneity. *Earth Planet. Sci. Lett.* **357-358**, 68–77 (2012).
19. Ford, H. A., Long, M. D., He, X. & Lynner, C. Lowermost mantle flow at the eastern edge of the African Large Low Shear Velocity Province. *Earth Planet. Sci. Lett.* **420**, 12–22, DOI: [10.1016/j.epsl.2015.03.029](https://doi.org/10.1016/j.epsl.2015.03.029) (2015).
20. Wolf, J., Li, M., Haws, A. A. & Long, M. D. Strong seismic anisotropy due to upwelling flow at the root of the Yellowstone mantle plume. *Geology* DOI: [10.1130/G51919.1](https://doi.org/10.1130/G51919.1) (2024).
21. Nowacki, A., Wookey, J. & Kendall, J.-M. Deformation of the lowermost mantle from seismic anisotropy. *Nature* **467**, 1091–1094, DOI: [10.1038/nature09507](https://doi.org/10.1038/nature09507) (2010).
22. Dziewonski, A. M. & Anderson, D. L. Preliminary reference Earth model. *Phys. Earth Planet. Interiors* **25**, 297–356, DOI: [10.1016/0031-9201\(81\)90046-7](https://doi.org/10.1016/0031-9201(81)90046-7) (1981).

23. Wang, Y. & Wen, L. Mapping the geometry and geographic distribution of a very low velocity province at the base of the Earth's mantle. *J. Geophys. Res. Solid Earth* **109**, DOI: [10.1029/2003JB002674](https://doi.org/10.1029/2003JB002674) (2004).
24. Tesoniero, A., Leng, K., Long, M. D. & Nissen-Meyer, T. Full wave sensitivity of SK(K)S phases to arbitrary anisotropy in the upper and lower mantle. *Geophys. J. Int.* **222**, 412 – 435, DOI: [10.1093/gji/ggaa171](https://doi.org/10.1093/gji/ggaa171) (2020).
25. Wolf, J., Long, M. D., Leng, K. & Nissen-Meyer, T. Constraining deep mantle anisotropy with shear wave splitting measurements: Challenges and new measurement strategies. *Geophys. J. Int.* **230**, 507–527, DOI: [10.1093/gji/ggac055](https://doi.org/10.1093/gji/ggac055) (2022).
26. Yuan, H. & Romanowicz, B. Lithospheric layering in the North American Craton. *Nature* **466**, 1063–1068, DOI: [10.1038/nature09332](https://doi.org/10.1038/nature09332) (2010).
27. Creasy, N., Long, M. D. & Ford, H. A. Deformation in the lowermost mantle beneath Australia from observations and models of seismic anisotropy. *J. Geophys. Res. Solid Earth* **122**, 5243–5267, DOI: [10.1002/2016JB013901](https://doi.org/10.1002/2016JB013901) (2017).
28. Deng, J. *et al.* Lowermost mantle anisotropy near the eastern edge of the Pacific LLSVP: constraints from SKS-SKKS splitting intensity measurements. *Geophys. J. Int.* **210**, 774–786, DOI: [10.1093/gji/ggx190](https://doi.org/10.1093/gji/ggx190) (2017).
29. Nowacki, A. & Wookey, J. The limits of ray theory when measuring shear wave splitting in the lowermost mantle with ScS waves. *Geophys. J. Int.* **207**, 1573–1583, DOI: [10.1093/gji/ggw358](https://doi.org/10.1093/gji/ggw358) (2016).
30. Parisi, L., Ferreira, A. M. G. & Ritsema, J. Apparent Splitting of S Waves Propagating Through an Isotropic Lowermost Mantle. *J. Geophys. Res. Solid Earth* **123**, 3909–3922, DOI: [10.1002/2017JB014394](https://doi.org/10.1002/2017JB014394) (2018).
31. Wolf, J. & Long, M. ScS shear-wave splitting in the lowermost mantle: Practical challenges and new global measurements. *Seismica* DOI: [10.26443/seismica.v3i1.1128](https://doi.org/10.26443/seismica.v3i1.1128) (2024).

32. Wolf, J., Long, M. D. & Frost, D. A. Ultralow velocity zone and deep mantle flow beneath the Himalayas linked to subducted slab. *Nat. Geosci.* 1–7, DOI: [10.1038/s41561-024-01386-5](https://doi.org/10.1038/s41561-024-01386-5) (2024).
33. Wolf, J., Long, M. D., Creasy, N. & Garnero, E. On the measurement of Sdiff splitting caused by lowermost mantle anisotropy. *Geophys. J. Int.* DOI: [10.1093/gji/ggac490](https://doi.org/10.1093/gji/ggac490) (2023).
34. Steinberger, B. Plumes in a convecting mantle: Models and observations for individual hotspots. *J. Geophys. Res. Solid Earth* **105**, 11127–11152, DOI: [10.1029/1999JB900398](https://doi.org/10.1029/1999JB900398) (2000).
35. French, S. W. & Romanowicz, B. A. Whole-mantle radially anisotropic shear velocity structure from spectral-element waveform tomography. *Geophys. J. Int.* **199**, 1303–1327, DOI: [10.1093/gji/ggu334](https://doi.org/10.1093/gji/ggu334) (2014).
36. van der Meer, D. G., van Hinsbergen, D. J. & Spakman, W. Atlas of the underworld: Slab remnants in the mantle, their sinking history, and a new outlook on lower mantle viscosity. *Tectonophysics* **723**, 309–448 (2018).
37. Lithgow-Bertelloni, C. & Richards, M. A. The dynamics of cenozoic and mesozoic plate motions. *Rev. Geophys.* **36**, 27–78, DOI: [10.1029/97RG02282](https://doi.org/10.1029/97RG02282) (1998).
38. Garnero, E. & McNamara, A. Structure and Dynamics of Earth's Lower Mantle. *Science* **320**, 626–628, DOI: [10.1126/science.1148028](https://doi.org/10.1126/science.1148028) (2008).
39. Long, M. D. & Lynner, C. Seismic anisotropy in the lowermost mantle near the Perm Anomaly. *Geophys. Res. Lett.* **42**, 7073–7080, DOI: [10.1002/2015GL065506](https://doi.org/10.1002/2015GL065506) (2015).
40. Tao, J., Hu, J., Jin, C. & He, X. Seismic evidence links the subducted Mongol-Okhotsk slab to deformation in D'' near the northeastern margin of the Perm Anomaly. *Tectonophysics* **774**, 228297, DOI: [10.1016/j.tecto.2019.228297](https://doi.org/10.1016/j.tecto.2019.228297) (2020).
41. Wolf, J., Creasy, N., Pisconti, A., Long, M. D. & Thomas, C. An investigation of seismic anisotropy in the lowermost mantle beneath Iceland. *Geophys. J. Int.* **219**, S152 – S166, DOI: [10.1093/gji/ggz312](https://doi.org/10.1093/gji/ggz312) (2019).

42. Chandler, B. C., Chen, L.-W., Li, M., Romanowicz, B. & Wenk, H.-R. Seismic anisotropy, dominant slip systems and phase transitions in the lowermost mantle. *Geophys. J. Int.* **227**, 1665–1681, DOI: [10.1093/gji/ggab278](https://doi.org/10.1093/gji/ggab278) (2021).
43. Wenk, H.-R., Cottaar, S., Tomé, C. N., McNamara, A. & Romanowicz, B. Deformation in the lowermost mantle: From polycrystal plasticity to seismic anisotropy. *Earth Planet. Sci. Lett.* **306**, 33–45, DOI: [10.1016/j.epsl.2011.03.021](https://doi.org/10.1016/j.epsl.2011.03.021) (2011).
44. Cottaar, S., Li, M., McNamara, A. K., Romanowicz, B. & Wenk, H.-R. Synthetic seismic anisotropy models within a slab impinging on the core–mantle boundary. *Geophys. J. Int.* **199**, 164–177, DOI: [10.1093/gji/ggu244](https://doi.org/10.1093/gji/ggu244) (2014).
45. Koelemeijer, P., Schuberth, B., Davies, D., Deuss, A. & Ritsema, J. Constraints on the presence of post-perovskite in Earth’s lowermost mantle from tomographic–geodynamic model comparisons. *Earth Planet. Sci. Lett.* **494**, 226–238, DOI: [10.1016/j.epsl.2018.04.056](https://doi.org/10.1016/j.epsl.2018.04.056) (2018).
46. Murakami, M., Hirose, K., Kawamura, K., Sata, N. & Ohishi, Y. Post-Perovskite Phase Transition in MgSiO₃. *Science* **304**, 855–858, DOI: [10.1126/science.1095932](https://doi.org/10.1126/science.1095932) (2004).
47. Nowacki, A. & Cottaar, S. *Toward Imaging Flow at the Base of the Mantle with Seismic, Mineral Physics, and Geodynamic Constraints*, chap. 13, 329–352 (American Geophysical Union (AGU), 2021).
48. Wu, X. *et al.* Seismic anisotropy of the D'' layer induced by (001) deformation of post-perovskite. *Nat. Commun.* DOI: [10.1038/ncomms14669](https://doi.org/10.1038/ncomms14669) (2017).
49. Li, M., Wolf, J., Garnero, E. & Long, M. D. Flow and Deformation in Earth’s Deepest Mantle: Insights From Geodynamic Modeling and Comparisons With Seismic Observations. *J. Geophys. Res. Solid Earth* **129**, e2024JB029058, DOI: [10.1029/2024JB029058](https://doi.org/10.1029/2024JB029058) (2024).
50. Ward, J., Walker, A. M., Nowacki, A., Panton, J. & Davies, J. H. The sensitivity of lowermost mantle anisotropy to past mantle convection. *Phys. Earth Planet. Interiors* **356**, 107264, DOI: [10.1016/j.pepi.2024.107264](https://doi.org/10.1016/j.pepi.2024.107264) (2024).

51. Vinnik, L., Farra, V. & Romanowicz, B. Azimuthal anisotropy in the earth from observations of SKS at GEOSCOPE and NARS broadband stations. *Bull. - Seismol. Soc. Am.* **79**, 1542–1558, DOI: [10.1785/BSSA0790051542](https://doi.org/10.1785/BSSA0790051542) (1989b).
52. Silver, P. G. & Chan, W. W. Shear wave splitting and subcontinental mantle deformation. *J. Geophys. Res. Solid Earth* **96**, 16429–16454, DOI: [10.1029/91JB00899](https://doi.org/10.1029/91JB00899) (1991).
53. Chevrot, S. Multichannel analysis of shear wave splitting. *J. Geophys. Res. Solid Earth* **105**, 21579–21590, DOI: [10.1029/2000JB900199](https://doi.org/10.1029/2000JB900199) (2000).
54. Link, F., Reiss, M. C. & Rumpker, G. An automatized XKS-splitting procedure for large data sets: Extension package for SplitRacer and application to the USArray. *Comput. & Geosci.* **158**, 104961, DOI: [10.1016/j.cageo.2021.104961](https://doi.org/10.1016/j.cageo.2021.104961) (2022).
55. Wolf, J., Becker, T. W., Garnero, E., Liu, K. H. & West, J. D. Comprehensive global dataset of 300,000 uniformly processed shear-wave splitting measurements with regular updates. *EarthArXiv* DOI: [10.31223/X54Q5S](https://doi.org/10.31223/X54Q5S) (2024).
56. Leng, K., Nissen-Meyer, T., van Driel, M., Hosseini, K. & Al-Attar, D. AxiSEM3D: broad-band seismic wavefields in 3-D global earth models with undulating discontinuities. *Geophys. J. Int.* **217**, 2125–2146, DOI: [10.1093/gji/ggz092](https://doi.org/10.1093/gji/ggz092) (2019).
57. IRIS Transportable Array. USArray Transportable Array, DOI: [10.7914/SN/TA](https://doi.org/10.7914/SN/TA) (2003).
58. Ekström, G., Nettles, M. & Dziewoński, A. The global CMT project 2004–2010: Centroid-moment tensors for 13,017 earthquakes. *Phys. Earth Planet. Interiors* **200**, 1–9, DOI: [10.1016/j.pepi.2012.04.002](https://doi.org/10.1016/j.pepi.2012.04.002) (2012).
59. Karato, S.-i. *Deformation of Earth Materials: An Introduction to the Rheology of Solid Earth* (Cambridge University Press, 2008).
60. Walker, A. & Wookey, J. MSAT - a new toolkit for the analysis of elastic and seismic anisotropy. *Comput. Geosci.* **49**, 81–90, DOI: [10.1016/j.cageo.2012.05.031](https://doi.org/10.1016/j.cageo.2012.05.031) (2012).
61. Browaeys, J. T. & Chevrot, S. Decomposition of the elastic tensor and geophysical applications. *Geophys. J. Int.* **159**, 667–678, DOI: [10.1111/j.1365-246X.2004.02415.x](https://doi.org/10.1111/j.1365-246X.2004.02415.x) (2004).

62. Fernando, B. *et al.* AxiSEM3D - an introduction to using the code and its applications. *EarthArXiv*
DOI: [10.31223/X5TH7P](https://doi.org/10.31223/X5TH7P) (2024).

Corresponding author

Correspondence to Jonathan Wolf (jonathan.wolf@berkeley.edu).

Acknowledgements

JW was funded by the Miller Institute for Basic Research in Science at UC Berkeley. BAR, EG, and JDW received support from the National Science Foundation via grants No. EAR-2054951, EAR-1855624, and EAR-1853911. JW acknowledges discussions with Regina Maass and Annie Haws.

Data availability

All data used in this study are publicly available and were collected and pre-processed as part of ASU's global data collection system (<http://adept.sese.asu.edu/>) for their global data products project (<http://swat.sese.asu.edu>). More details are specified in the Supplementary Information.

Code availability

Shear-wave splitting measurements were conducted using SplitRacer_auto⁵⁴, available at <https://www.geophysik.uni-frankfurt.de/64002762/Software>. Synthetic seismograms for this study were computed using AxiSEM3D, which is publicly available at <https://github.com/AxiSEMunity>⁶².

Author contributions statement

Conceptualization: JW; Data analysis and synthetic modeling: JW; Methodology: JW, BAR, EG; Visualization: JW, EG; Writing and editing: JW, BAR, EG, WZ, JDW; Resources: JW, BAR, EG, WZ.; Data collection: JDW.

Competing Interests

The authors declare no competing interests relevant to this work.

1 Patterns of deformation in the deepest mantle linked 2 to ancient subduction – Supplementary Information

3 Jonathan Wolf^{1,2,*}, Barbara A. Romanowicz¹, Edward Garnero³, Weiqiang Zhu¹, and John
4 D. West³

5 ¹Department of Earth and Planetary Science, University of California, Berkeley, CA, USA

6 ²Miller Institute for Basic Research in Science, Berkeley, CA, USA

7 ³School of Earth and Space Exploration, Arizona State University, Tempe, AZ, USA

8 *jonathan.wolf@berkeley.edu

9 10 11 Tomography models used for the vote map of Figure 4b

12 Seismic tomography models used to create the shear velocity vote map of Figure 4b in the main manuscript are GyPSuM⁶³,
13 Savani⁶⁴, SEMUCB-WM1⁶⁵, S40RTS⁶⁶ and SGLOBE-rani⁶⁷.

14 Utilized Data

15 Data were collected from the following on-line data centers: AUSPASS (<https://auspass.edu.au/data.html>),
16 BGR (<https://eida.bgr.de/>), CNDC ([https://www.earthquakescanada.nrcan.gc.ca/stndon/CNDC/
17 index-en.php](https://www.earthquakescanada.nrcan.gc.ca/stndon/CNDC/index-en.php)), Earthscope (<http://service.iris.edu/>), ETH (<https://eida.ethz.ch/>), FNET (<https://www.fnet.bosai.go.jp/top.php?LANG=en>), GEOFON (<https://geofon.gfz-potsdam.de/>)⁶⁸, GDMS
18 (<https://gdmsn.cwb.gov.tw/>)⁶⁹, ICGC ([https://www.icgc.cat/en/Ciutada/Explora-Catalunya/
19 Terratremols](https://www.icgc.cat/en/Ciutada/Explora-Catalunya/Terratremols)), INGV (http://cnt.rm.ingv.it/en/webservices_and_software), IPGP ([http://ws.
20 ipgp.fr/](http://ws.ipgp.fr/))⁷⁰, KNMI (<http://rdsa.knmi.nl/>), KOERI (<http://www.koeri.boun.edu.tr/new/en>), LMU
21 (<http://erde.geophysik.uni-muenchen.de/>), NCEDC (<https://ncedc.org/>)⁷¹, NIEP ([https://www.
22 infp.ro/](https://www.infp.ro/)), NOA (<http://bbnet.gein.noa.gr/HL/>), ORFEUS (<http://www.orfeus-eu.org/>), RESIF
23 (<https://seismology.resif.fr/>)⁷², SCEDC (<https://scedc.caltech.edu/>)⁷³, SSN ([http://www.ssn.
24 unam.mx/](http://www.ssn.unam.mx/))⁷⁴, TEXNET (<http://rtserve.beg.utexas.edu/>), and USP (<https://sismo.iag.usp.br/>).
25 All networks and network citations are included as Supplementary Information, and were derived from the FDSN network code
26 list (<https://fdsn.org/networks/>).
27

²⁸ **Codes used for basic seismological processing/figure creation**

²⁹ The Generic Mapping Tools⁷⁵, SubMachine⁷⁶, TauP⁷⁷ and ObsPy⁷⁸ were used in this study.

Supplementary Figures

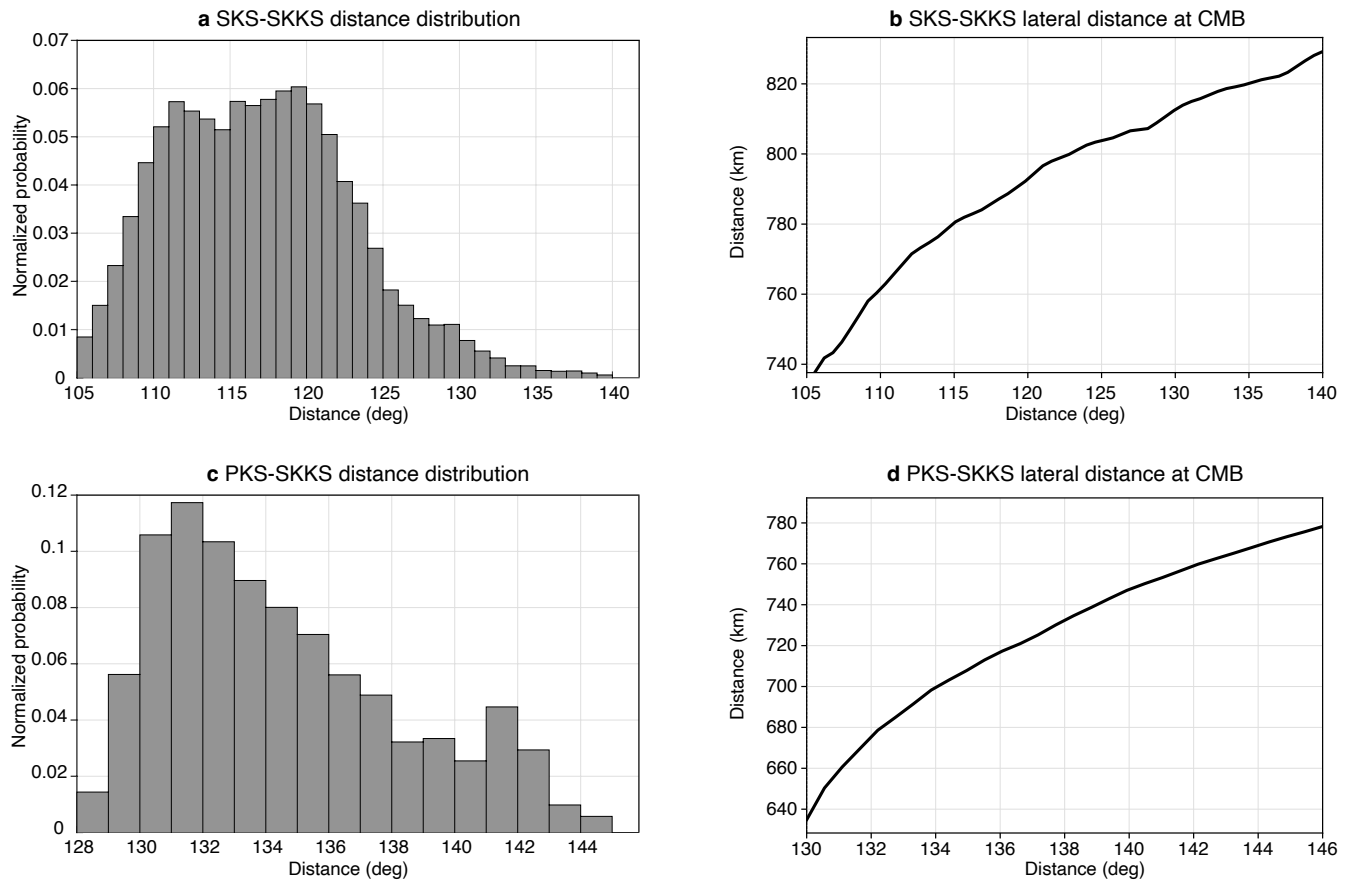


Figure S1. Epicentral distance distribution of measurements and lateral distance between *KS phase pairs at the core-mantle boundary (CMB). **a** Epicentral distance distribution for all SKS-SKKS differential splitting measurements. **b** Distance at the core-mantle boundary between SKS-SKKS pairs as a function of epicentral distance. **c** Same as panel **a** for PKS-SKKS. **d** Same as panel **b** for PKS-SKKS.

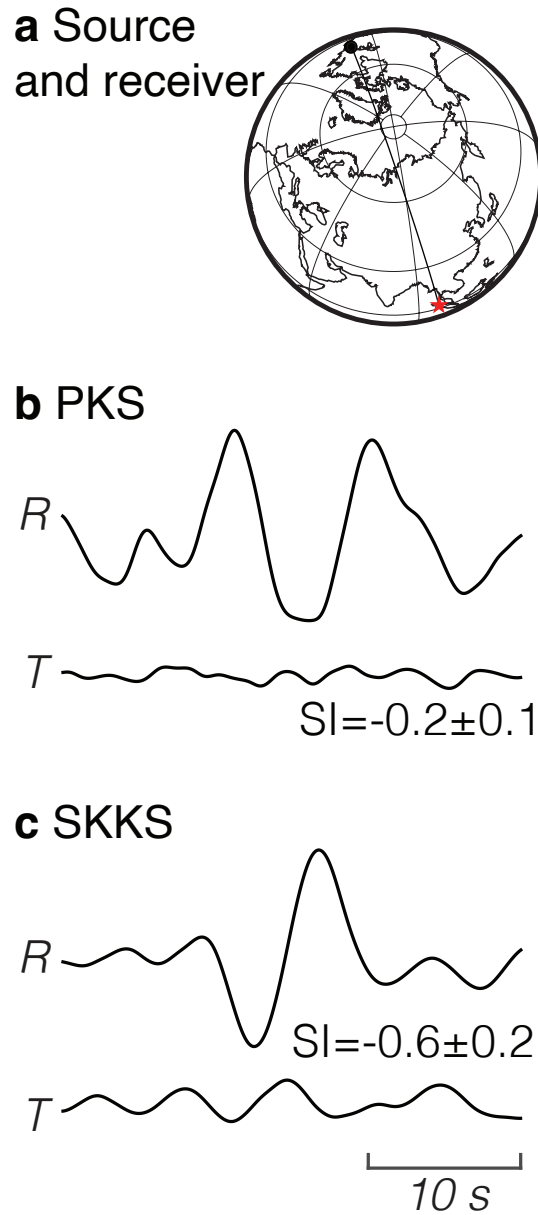


Figure S2. Differential PKS-SKKS splitting example. **a** The measurement was made for event (red star) that occurred on September 5, 2011 and was recorded at station SSPA (black star). **b** PKS radial (R) and transverse (T) seismograms. **c** Same for SKKS. The splitting intensity difference between PKS and SKKS is 0.4.

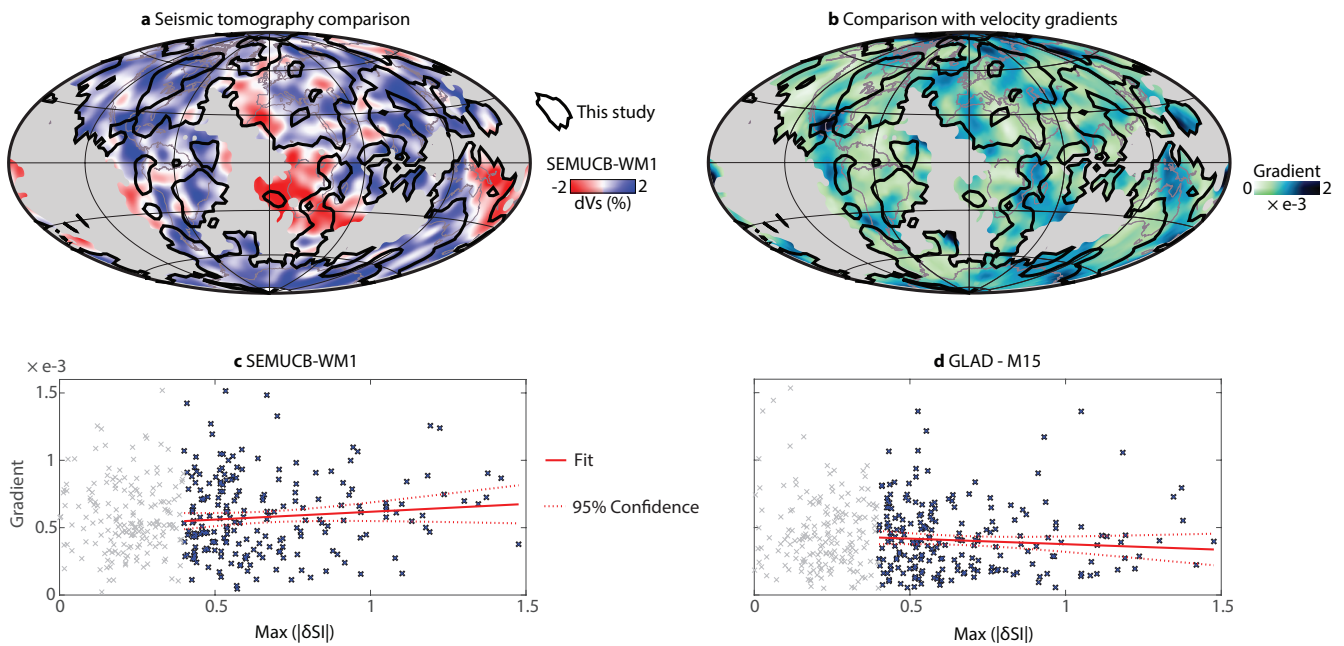


Figure S3. Comparisons of the seismic anisotropy results to seismic tomography models. (a) Shear velocity perturbations (legend) according to SEMUCB-WM1 at 2800 km depth. Gray colors indicate regions without coverage. Black outlines show regions with $\text{Max } |\delta SI| > 0.4$. (b) Similar plotting conventions as panel (a) but showing lateral velocity gradients of SEMUCB-WM1. (c) Relationship between lateral seismic velocity gradients and $\text{Max } |\delta SI|$ for SEMUCB-WM1. $\text{Max } |\delta SI|$ are plotted as gray (≤ 0.4) and black (> 0.4) crosses. A linear fit is shown as a solid red line, and 95% confidence bounds are represented as solid dashed lines. (d) Same as panel (c) for GLAD-M15⁷⁹.

References

63. Simmons, N. A., Forte, A. M., Boschi, L. & Grand, S. P. GyPSuM: A joint tomographic model of mantle density and seismic wave speeds. *J. Geophys. Res. Solid Earth* **115**, DOI: [10.1029/2010JB007631](https://doi.org/10.1029/2010JB007631) (2010).
64. Auer, L., Boschi, L., Becker, T. W., Nissen-Meyer, T. & Giardini, D. Savani: A variable resolution whole-mantle model of anisotropic shear velocity variations based on multiple data sets. *J. Geophys. Res. Solid Earth* **119**, 3006–3034 (2014).
65. French, S. W. & Romanowicz, B. A. Whole-mantle radially anisotropic shear velocity structure from spectral-element waveform tomography. *Geophys. J. Int.* **199**, 1303–1327, DOI: [10.1093/gji/ggu334](https://doi.org/10.1093/gji/ggu334) (2014).
66. Ritsema, J., Deuss, A., van Heijst, H. J. & Woodhouse, J. H. S4ORTS: a degree-40 shear-velocity model for the mantle from new Rayleigh wave dispersion, teleseismic traveltimes and normal-mode splitting function measurements. *Geophys. J. Int.* **184**, 1223–1236, DOI: [10.1111/j.1365-246X.2010.04884.x](https://doi.org/10.1111/j.1365-246X.2010.04884.x) (2011).
67. Chang, S.-J., Ferreira, A. M. G., Ritsema, J., van Heijst, H. J. & Woodhouse, J. H. Joint inversion for global isotropic and radially anisotropic mantle structure including crustal thickness perturbations. *J. Geophys. Res. Solid Earth* **120**, 4278–4300, DOI: [10.1002/2014JB011824](https://doi.org/10.1002/2014JB011824) (2015).
68. GFZ Data Services. GEOFON Data Centre: GEOFON Seismic Network, DOI: [10.14470/TR560404](https://doi.org/10.14470/TR560404) (1993).
69. Central Weather Bureau (CWB), T. Central Weather Bureau Seismographic Network, DOI: [10.7914/SN/T5](https://doi.org/10.7914/SN/T5) (2012).
70. Institut de physique du globe de Paris (IPGP) & École et Observatoire des Sciences de la Terre de Strasbourg (EOST). Geoscope, french global network of broad band seismic stations, DOI: [10.18715/GEOSCOPE.G](https://doi.org/10.18715/GEOSCOPE.G) (1982).
71. UC Berkeley Seismological Laboratory. Northern California Earthquake Data Center, DOI: [10.7932/NCEDC](https://doi.org/10.7932/NCEDC) (2014).
72. RESIF. RESIF-RLBP French Broad-band network, RESIF-RAP strong motion network and other seismic stations in metropolitan France, DOI: [10.15778/RESIF.FR](https://doi.org/10.15778/RESIF.FR) (1995).
73. Caltech. Southern California Earthquake Center, DOI: [10.7909/C3WD3xH1](https://doi.org/10.7909/C3WD3xH1) (2014).
74. Instituto de Geofísica, Universidad Nacional Autónoma de México, México. SSN: Servicio Sismológico Nacional, DOI: [10.21766/SSNM/SN/MX](https://doi.org/10.21766/SSNM/SN/MX) (2024).
75. Wessel, P. & Smith, W. H. F. New, improved version of generic mapping tools released. *Eos, Transactions Am. Geophys. Union* **79**, 579–579, DOI: [10.1029/98EO00426](https://doi.org/10.1029/98EO00426) (1998).
76. Hosseini, K. *et al.* SubMachine: Web-Based Tools for Exploring Seismic Tomography and Other Models of Earth's Deep Interior. *Geochem. Geophys. Geosystems* **19**, 1464–1483 (2018).
77. Crotwell, P., Owens, T. J. & Ritsema, J. The TauP Toolkit: Flexible Seismic Travel-Time and Raypath Utilities. *Seismol. Res. Lett.* **70**, DOI: [10.1785/gssrl.70.2.154](https://doi.org/10.1785/gssrl.70.2.154) (1999).
78. Beyreuther, M. *et al.* Obspy: A python toolbox for seismology. *Seismol. Res. Lett.* **81**, 530–533, DOI: [10.1111/10.1785/gssrl.81.3.530](https://doi.org/10.1111/10.1785/gssrl.81.3.530) (2010).

62 **79.** Bozdağ, E. *et al.* Global adjoint tomography: first-generation model. *Geophys. J. Int.* **207**, 1739 – 1766, DOI: [10.1093/gji/](https://doi.org/10.1093/gji/ggw356)
63 [ggw356](https://doi.org/10.1093/gji/ggw356) (2016).